Towards retrieving distributed aquifer hydraulic parameters from distributed strain sensing

Yi Zhang[1], Xinglin Lei[2], Tsutomu Hashimoto[1], and Ziqiu Xue[3]

[1]Geological Carbon Dioxide Storage Technology Research Association, Kyoto, 6190292 Japan.
[2]Geological Survey of Japan, National Institute of Advanced Industrial Science and Technology, Tsukuba, 305-8567, Japan
[3]Geological Carbon Dioxide Storage Technology Research Association, Kyoto, 6190292 Japan

November 21, 2022

Abstract

Subtle elastic rock deformation during aquifer testing may bear hydraulic parameter (permeability and compressibility) information owing to the poroelastic hydromechanical coupling effect. Here we report that such in situ rock deformations (~50 με) during an aquifer pumping test are successfully measured along a vertical well by a high-resolution fiber optic distributed strain sensing (DSS) tool with an accuracy of 0.5 με. We investigate the feasibility of hydraulic parameter estimation at meter scale using DSS data through a coupled hydromechanical model. Both synthetic and field cases are tested with sensitivity analysis. The results indicate that the simultaneous estimation of permeability and compressibility using DSS data is possible at low noise levels. However, only non-global near-optimal solutions can be obtained using the applied gradient-based inversion algorithm, because of parameter crosstalk and sensitivity problems when the data contain large noise. In particular, estimation is difficult for zones with relatively low permeability due to the low sensitivity to the strain changes. The estimated permeability/compressibility structures for the field test are largely consistent with other geological information from well logs. Our study suggests that DSS data can be quite useful in aquifer characterization and fluid flow profiling in addition to geomechanical monitoring. The obtained hydraulic information is beneficial for the optimized reservoir management of water and oil/gas storage.

Hosted file

essoar.10505365.1.docx available at https://authorea.com/users/532022/articles/597797-towards-retrieving-distributed-aquifer-hydraulic-parameters-from-distributed-strain-sensing

Towards retrieving distributed aquifer hydraulic parameters from distributed strain sensing

Yi Zhang[1, 2 *], Xinglin Lei[3], Tsutomu Hashimoto[1, 2], Ziqiu Xue[1, 2]

Corresponding author: zhangyi@rite.or.jp

[1] Geological Carbon Dioxide Storage Technology Research Association, 9-2, Kizugawadai, Kizugawa-Shi, Kyoto, 619-0292 Japan.

[2] Research Institute of Innovative Technology for the Earth (RITE), 9-2, Kizugawadai, Kizugawa-Shi, Kyoto, 619-0292 Japan.

[3] Geological Survey of Japan, National Institute of Advanced Industrial Science and Technology, AIST Central #7, Higashi 1-1-1, Tsukuba, Ibaraki 305-8567, Japan.

Key Points:

- Small poroelastic deformation during aquifer testing was monitored using a high-resolution distributed strain sensing (DSS) tool.
- DSS data are used to inversely estimate the vertical profiles of permeability and compressibility through a coupled hydromechanical model.
- DSS and inverse modeling are useful for subsurface reservoir characterization and management.

Abstract

Subtle elastic rock deformation during aquifer testing may bear hydraulic parameter (permeability and compressibility) information owing to the poroelastic hydromechanical coupling effect. Here we report that such in situ rock deformations (~50 με) during an aquifer pumping test are successfully measured along a vertical well by a high-resolution fiber optic distributed strain sensing (DSS) tool with an accuracy of 0.5 με. We investigate the feasibility of hydraulic parameter estimation at meter scale using DSS data through a coupled hydromechanical model. Both synthetic and field cases are tested with sensitivity analysis. The results indicate that the simultaneous estimation of permeability and compressibility using DSS data is possible at low noise levels. However, only non-global near-optimal solutions can be obtained using the applied gradient-based inversion algorithm, because of parameter crosstalk and sensitivity problems when the data contain large noise. In particular, estimation is difficult for zones with relatively low permeability due to the low sensitivity to the strain changes. The estimated permeability/compressibility structures for the field test are largely consistent with other geological information from well logs. Our study suggests that DSS data can be quite useful in aquifer characterization and fluid flow profiling in addition to geomechanical monitoring. The obtained hydraulic information is beneficial for the optimized reservoir management of water and oil/gas storage.

Plain Language Summary

Permeability and compressibility are the two most important hydraulic parameters used in reservoir models for understanding fluid flow behavior. The parameters control the evolution of pore pressure, fluid flow, and coupled deformation in the reservoir. The resultant strain records may contain the information of pore pressure and fluid flow. In this study, we tested the feasibility of simultaneously estimating permeability and compressibility of a multi-layered

aquifer using the distributed strain data and a hydromechanically coupled model. The results show that the compressibility and permeability of zones with high permeability can be generally well resolved in the estimation, for they have higher sensitivity to the strain changes, whereas the permeability of zones with relatively lower permeability cannot be well constrained because of the low sensitivity to strain changes. Using the high-fidelity field records of distributed strain data (with an accuracy of 0.5 $\mu\varepsilon$) in the aquifer pumping test, we constructed the profiles of permeability and compressibility, which are largely consistent with other geological information. Our study provides a new method for reservoir characterization and is useful for optimized reservoir management.

1 Introduction

Permeability and compressibility (or hydraulic conductivity and specific storage) are two of the most important hydraulic parameters for modeling fluid flow behavior in underground reservoirs (Anderson et al., 2015; Bear & Verruijt, 2012). A better understanding of the spatial distribution of hydraulic parameters can facilitate more manageable and optimized operations for these utilizations (Miller et al., 2017). Moreover, the parameters are essential for understanding the scale of hydromechanical responses and its role in fluid injection induced seismicity (Guglielmi et al., 2020; Jiang et al., 2020; Shirzaei et al., 2016; Verdon et al., 2015; Keranen et al., 2014; Lei et al., 2020). Hydrogeologists have long pursued an understanding of the spatial structure of hydraulic parameters in aquifer formation. These efforts can be classified into three categories: (1) hydraulic methods; (2) geophysical methods; and (3) geodetic deformation-based methods.

The first category includes hydraulic pumping, slug, tracer, and hydraulic tomographic testing methods (Istok & Dawson, 2014; Yeh & Liu, 2000). Among the methods, the pumping test is suggested to be the most reliable method for determining aquifer permeability and compressibility. However, usually only a pair of permeability and compressibility values of the entire aquifer section can be obtained. Beside purposed pumping tests, even natural tidal force induced hydraulic response can be used for parameter estimation (e.g. Hsieh et al., 1987; Wang et al., 2018). The hydraulic tomography (HT) method is a tomographic approach that inversely reconstructs parameter fields using information from multiple hydraulic head (or pressure) records. The promising performance of HT has been documented in many studies even for heterogeneous aquifers (Gottlieb & Dietrich, 1995; Hochstetler et al., 2016; Jiménez et al., 2015; Vasco, 2018; Vasco et al., 2019). However, the method performance greatly depends on data acquisition and the quality of the assumed geostatistical priors (Kitanidis, 1997). Because of the spatial limitation in hydraulic head measurements, the inverted parameter field is often overly smoothed and the model assessment for determining model resolution is required (Aster et al., 2018; Menke, 2018; Vasco et al., 1997). The second category of methods indirectly provides permeability or compressibility data from geophysical parameters, such as electrical resistivity, temperature, or acoustic velocity that are obtained from well logging, cross-well or surface geophysical surveys (Huntley, 1986; Yamamoto et al., 1995). These geophysical parameters usually have a relatively weak physical-constrained relationship with hydraulic parameters. The estimation might be less quantitative compared with the first category. A joint inversion of multi-physical data has been used to give a better parameter characterization (e.g. Commer et al., 2020; Jardani & Revil 2009; Liang et al., 2016).

With the advance of space observation technologies, a third category of methods, based on the geodetic observations of earth surface deformations, have been developed to constrain or estimate hydraulic parameters on a large scale. For example, the interferometric synthetic-aperture radar (InSAR) technique and Global Navigation Satellite System (GNSS) method have been applied to monitor the surface deformation caused by underground fluid extractions or injections and obtain the lateral permeability distribution of underground reservoirs over a large area (Alghamdi et al., 2020; Bohloli et al., 2018; Comola et al., 2016; Shirzaei et al., 2019; Vasco et al., 2008, 2010). Despite the progress made, to date, it remains a challenge to characterize fine-scale hydraulic parameters in the vertical direction. A fine-scale characterization of hydraulic parameters is essential for the manageable and optimized utilization of subsurface reservoirs through numerical modeling.

The feasibility and performance of DSS for reservoir formation deformation monitoring have been shown in several recent field studies (Lei et al., 2019; Sun et al., 2019). Using a high-resolution DSS tool, Zhang et al. (2019) and Zhang & Xue (2019) conducted laboratory tests to demonstrate that quasi-static deformation field accompanying fluid injection and pore pressure changes in reservoir rocks can be deployed to monitor fluid plume migration and gain information on rock permeability and compressibility. More recently, Becker et al. (2020) reported successful field experiments using DSS to monitor the displacement in fractured formation due to hydraulic pressure stimulation.

In this paper, we investigate the feasibility of using distributed strain data to estimate the distributed hydraulic parameters with a coupled poroelastic model and a gradient-based inversion algorithm. We first present a set of high-fidelity strain records from successful DSS application in the monitoring of a field-scale aquifer pumping test. Then we provide the methods of the forward and inverse modeling. Finally, we apply the methods to the synthetic and field studies and present the one-dimensional meter-scale profiles of permeability and compressibility obtained using the proposed inversion method. We also discussed the limitation of the method due to parameter crosstalk and noise.

2. Aquifer pumping test with distributed strain sensing

2.1 Test site and operations

We conducted an aquifer pumping test in the rural area of Mobara City, Chiba, Japan. Pressure drawdown-induced in situ formation deformation was monitored by a downhole-installed high-resolution fiber optic DSS system. The target aquifer of the site was shallow at approximately ~300 m deep. The aquifer had a simple hydrostratigraphic setting with alternation strata of sandstone, mud and siltstone (Figure S1), which were formed in a shelf-margin delta environment. In the past, the overexploitation of groundwater to extract dissolved natural gas and iodine, agricultural irrigation, and other industrial utilizations have caused ground subsidence in Chiba (Horiguchi, 1998). Since the 1970s, because of more severe regulations and reinjection, subsidence has been largely mitigated. In this study, the water extraction depths (approximately 161–240 m) were fully perforated and belong to the Chonan Formation (Middle Pleistocene). There is no evidence of existing fractures in the formation. In a previous study, Lei et al. (2019) estimated the permeability of the entire formation to be approximately 470 mD. However, permeability remains unclear for each depth. Aquifer water resources are frequently exploited during spring and summer for agricultural irrigation. To avoid interference, the water pumping test was performed in November. An existing agricultural well (Well1) was used for water pumping. A monitoring well (Well2) equipped with optical fiber cables was located 175.1 m away from the pumping well. Optical fiber cables were installed behind the well casing and grouted in the cement annulus between the casing and aquifer formation. Another well (Well3) located 5.5 m away from the monitoring well was perforated between depths of 186.8 and 193.6 m, which was used to monitor water head change.

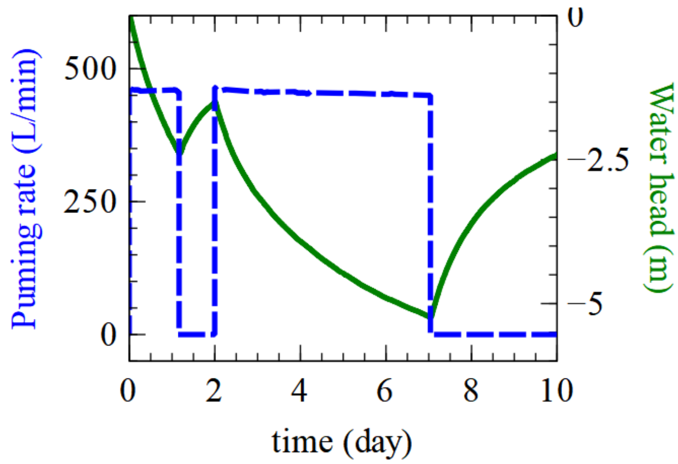

Figure 1. Recorded field data of water pumping rate and changes in water head.

Water extraction was conducted for approximately 7 days within the depth range of the Chonan formation (Figure 1). There were two main pumping operation steps: (1) the initial pumping (460 L/min) with the drawdown of the water head (lasting approximately 1.2 days), which involved a temporary pause with the partial recovery of water head (approximately 0.8 days), and pumping (450 L/min) with the drawdown of water head (approximately 5 days), and (2) the end of pumping and subsequent final recovery. In this study, we focused only on the pumping stage. The fiber optic acquisition was performed using the Neubrescope NBX-8000 device and the Tunable Wavelength Coherent Optical Time Domain Reflectometry (TW-COTDR) method (Kishida et al., 2014; Zhang et al., 2020). Continuous and distributed strain data with an accuracy of 0.5 με, spatial resolution of 5 cm and a time resolution of approximately 1.1 hour was obtained during the entire pumping operation.

2.2 Distributed strain data

The distributed strain data obtained using DSS during the aquifer pumping test were plotted as a time–depth–value image, depth–value profiles, and time–value trend curves (Figure 2a–c). In Figure 2, the spatiotemporal changes in strain responses during water extraction at the well location with the installed optical fiber cable can be observed. The strain changes are indicative of the impacted zones with aquifer pressure changes. The formation showed compressive deformations during the water extraction stages due to a reduction in the pore fluid pressure and effective stress, whereas it showed a temporal recovery (i.e., expansion deformation) during the extraction pause between the first and second operation days. With continued water extraction, the formation showed compressive deformations with gradually increasing magnitudes. The largest compressive strain developed in the final stage and was approximately 50 με, which is still considerably small. Along the vertical direction, variations in strain magnitude appear in different depths, which may indicate depth-dependent heterogeneities in permeability and compressibility. Particularly, large variations at several depths may indicate changes in the lithological structure (sandstone-mudstone alternations). Two sections (from 160 to 212 m and from 212 to 240 m) in the strain profile are distinguishable.

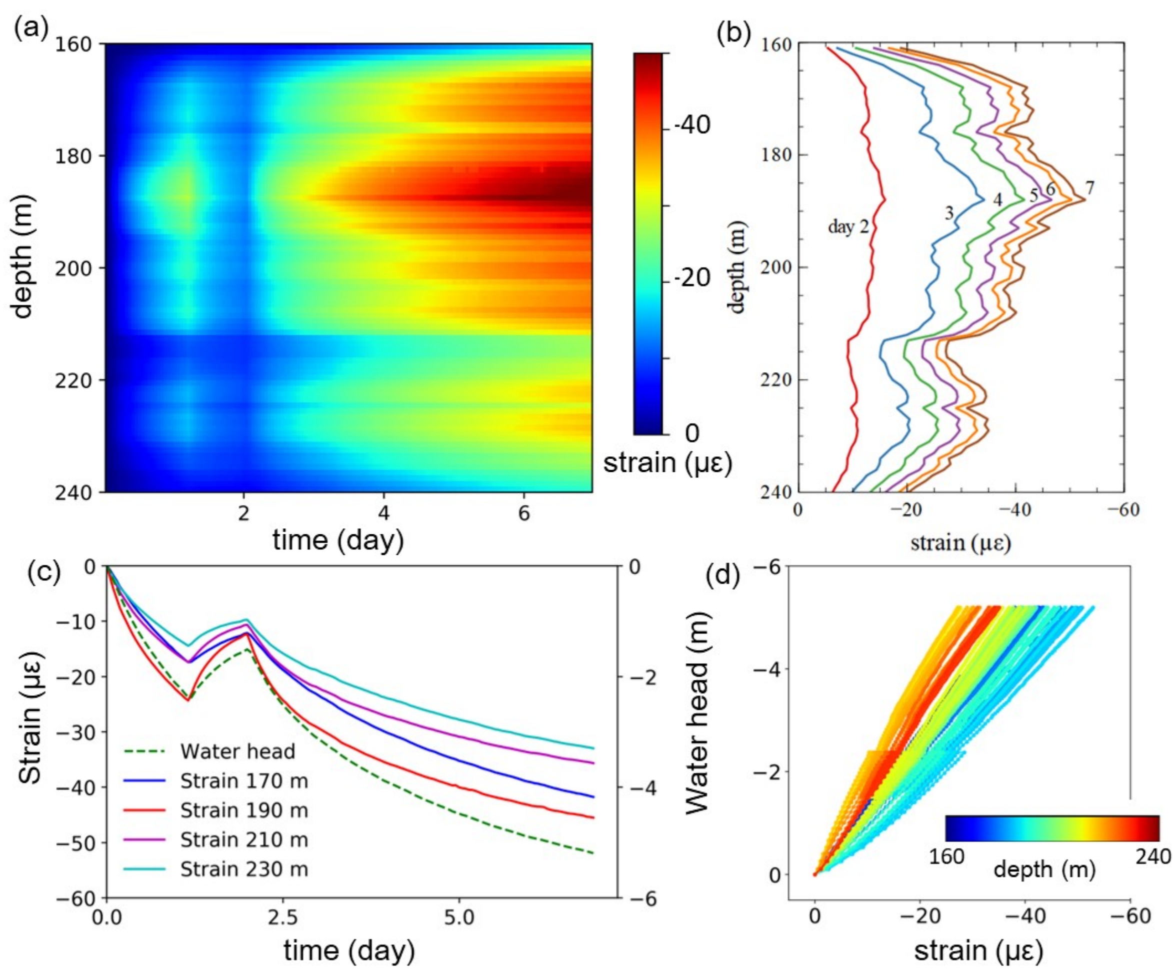

Figure 2. Vertical strain records at the observation well using distributed strain sensing during the aquifer test by water extraction. The data are presented in the forms of (a) image, (b) depth profiles, (c) time trends, and (d) cross plot with respect to water head. In (b), days 2 to 7 correspond to the x-axis of (a). In (d), only the depths between 170 and 230 m are plotted; linear trends are shown.

Most of the strain data (at each depth) exhibit trends that are similar to the water head (Figure 2c) with a nearly linear relationship (Figure 2d), which suggests linear poroelastic deformation in the aquifer formation. The strain changes monitored by DSS are representative of the deformation of aquifer formation due to a reduction in pressure. However, the depths near the top and bottom boundaries show a nonlinear trend (Figure S2), which could be related to the geomechanical effect. Most of the raw strain data (Figure S3) has smooth changes, which suggests high quality data with a good signal/noise ratio; a few data points have error spikes caused by incorrectly matching Rayleigh scattering power spectra using the cross-correlation method. We used a median filter to remove these spikes when preparing the data for the estimation of hydraulic parameters.

2.3 The benefits of DSS for reservoir geomechanics

The observations from DSS provide important constraints on the deformation in the vertical direction and are complementary to surface-based observations (e.g., InSAR), which have been used to monitor fluid migration and estimate lateral permeability distribution at large scales (Bohloli et al., 2018; Jha et al., 2015; Vasco et al., 2008). As shown by the data, even a small induced strain (~1 $\mu\varepsilon$) in the aquifer formation can be detected. This indicates that DSS should be useful for more detailed geomechanical studies, such as for tracking, evaluating, and managing aquifer deformation and understanding the role of underground deformation to surface subsidence. For instance, the extent of aquifer deformation due to seasonal massive agricultural irrigation can be evaluated in situ and in real time. The contribution of formation heterogeneity of each interval to total surface displacement and the mainly deforming parts can be understood by examining the local strain. Whether the aquifer has recovered to a normal state can be determined by checking the strain changes, by which the proper management of ground water resources is possible (Gleeson et al., 2012). Similar functionality could be utilized for CO_2 or natural gas storage in underground reservoirs. The real-time DSS data can offer accurate information to understand geomechanical deformation state as well as to evaluate geomechanical risk; it is also useful for tracking pressure and plume migrations (Zhang et al., 2019; Zhang & Xue, 2019; Murdoch et al., 2020).

3 From strain to hydraulic parameters: forward and inverse models

Beyond the above direct application of DSS related to geomechanical phenomena, the induced poroelastic deformation by formation pressure change may carry the information of hydraulic parameters. According to Biot's poroelastic theory, the hydromechanical coupling problems can be categorized as solid-to-fluid and fluid-to-solid (Wang, 2017). For example, consolidation induced excess fluid pressure and earthquake-driven fluid migration are solid-to-fluid coupling. Alternatively, fluid-to-solid coupling is usually used to describe changes in fluid pressure (due to injection or extraction) modifying the effective stress and deforming the rock. In the latter coupling, permeability and compressibility together control the evolution of pressure and strain. Inversely, by monitoring the strain changes of an aquifer, the fluid-to-solid coupling may provide an opportunity to characterize the two hydraulic parameters.

3.1 Forward model for poroelastic strain calculation

We employed a coupled hydromechanical model based on the poroelastic theory (Biot, 1941) to calculate strain due to hydraulic activities, e.g., aquifer pumping test. The main equations refer to those classic literatures (Biot, 1941; Cheng, 2016; Rice & Cleary, 1976; Wang, 2017). Through the forward problem solving the coupled hydromechanical equations with setting hydraulic and mechanical parameters, the spatial changes in stress, strain and pore pressure of the formation induced by water pumping can be calculated.

We constructed an axisymmetric cylinder two-dimensional model with Cartesian geometry (Figure 3), with the vertical axis representing the location of the pumping well to approximate the aquifer setting. To avoid possible impacts of boundary effects on strain changes in the testing region, which is the region of interest (ROI), we set a much larger modeling domain (500 × 500 m) than the ROI size (200 × 100 m) and set the boundary remote from the ROI. We used dense Cartesian mesh gridding (10 × 1 m) within the ROI and nearby regions and sparse gridding in outside regions. There were total 9,200 elements and approximately 28,000 of degree of freedom in the model. The injection section was between 161 and 240 m (80 m thick). The normal component of the displacements at the outer side and bottom of the model was set to 0. A Dirichlet constant pore pressure condition was set at the outer side. The water extraction source condition was set at the well boundary with time-dependent flux. The forward model starts from an initial hydrostatic equilibrium state; only the latter changes in pore pressure, stress and strain caused by water pumping were considered.

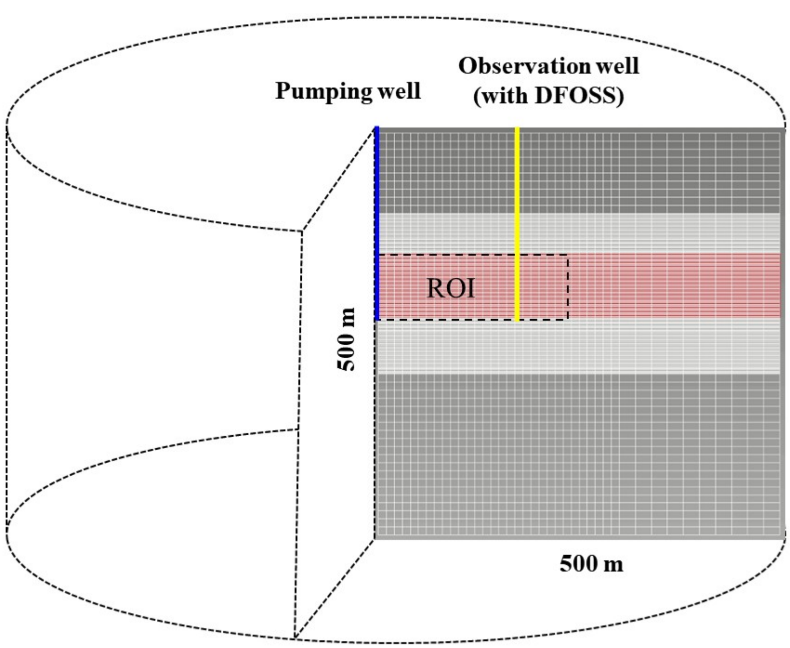

Figure 3. Schematic of the forward model.

In the hydromechanical model, we set one-dimensional layered variations (with a length interval of 1 m) of permeability (k) and compressibility (C_{α}), which are considered as the reciprocal of bulk modulus, within the ROI along the vertical direction. Following Lei et al., (2019), we applied uniform porosity (ϕ = 0.43), Biot's coefficient (α = 1), water compressibility ($C_f = 4.5\times10^{-10}$ 1/Pa), and Poisson's ratio (υ= 0.29) for all modeling. Only isotropic permeability and compressibility were considered. An observation well was located 175.1 m away from the pumping well. The same pumping rate in the field study was set. In this study, we only consider the vertical strain component, which is related to the DSS measurement. We have limited our study to the small and linear poroelastic deformation mechanism. We applied the open source finite element modeling framework MOOSE to solve the forward poroelastic model (Wilkins et al., 2020).

3.2 Inverse models for hydraulic parameter estimation from strain

The inverse problem is formulated by minimizing the objective function $f(x)$ accounting for the difference between the measured and modeled strain values:

$$minimize\, f(x) = \sum_{i=1}^{n} \left| \varepsilon_i(x) - \bar{\varepsilon}_i(x) \right| \qquad (1)$$

where $\bar{\varepsilon}_i$ and ε_i represent the measured and modeled strain values, respectively. There is a total of n = 80 × 2 unknowns (x) of permeability and compressibility for each layer (1 m thick) within the 80 m thickness formation. We provided an initial guess values (10 mD for the permeability and 1×10^{-9} 1/Pa for the compressibility) and bound constraints for the parameter ranges.

We used a nonlinear least-squares method with the trust region reflective algorithm (Branch et al., 1999) to solve the minimization problem (Virtanen et al., 2020). In the algorithm, the subset of the region of the nonlinear objective function (referred to as the trust region) can be approximated using a quadratic model function. The algorithm iteratively solves subspace problems in trust regions by the approximate Gauss–Newton method, with trust region shape and size determined by the distance from the bounds and the gradient direction. The algorithm considers search directions reflected from the bounds using a reflective transformation technique to improve convergence for problems with bound constraints; moreover it can properly handle bound constraints for large-scale nonlinear least-squares problems. For the method, it is necessary to calculate the objective function gradient (i.e. Jacobian matrix) and the Hessian matrix approximation. For the significant spatial heterogeneity and coupling nature in the model, the forward modeling by a single CPU is slow (~10 min). Accordingly, we used a supercomputer system (Oakbridge-CX Supercomputer System, University of Tokyo) to accelerate the Jacobian computation in parallel. We also used the Tikhonov regularization technique to condition the problem (e.g. by minimizing the sum of parameter gradient) and stabilize the estimation.

In principle, the inversion of hydraulic parameters using distributed strain data is similar to those used in the inversion of flow rate and permeability using distributed temperature sensing data (Becker et al., 2004; Maldaner et al., 2019; Medina et al., 2020). However, there are some inherent difficulties in the current inverse problem. The unknown parameters, permeability and compressibility, both influence the strain. They may have different sensitivities and numerical ranges that affect the strain changes; they may also have the parameter crosstalk (or trade-off) problem (Aster et al., 2018; Menke, 2018).

4 Hydraulic parameter estimation

4.1 Synthetic tests

We conducted numerical synthetic studies both with and without noise to examine the feasibility of the proposed method for inversely estimating hydraulic parameters using distributed strain data. In the synthetic model, the settings were the same as the latter modeling for the field study, but we set the synthetic model with assumed permeability and compressibility values (Figure 4a–b). By running the forward modeling once, we obtained synthetic transient strain records at each depth of the virtual observation well. For the case with noise, we added Gaussian random noise with a standard deviation (σ) of 0.5 (which corresponds to the measurement accuracy of the DSS tool in the field test), 2 and 5 με (approximately 10% of the average strain for the record at the zone with lowest strain). Permeability and compressibility were then set in the formation as unknowns and estimated inversely by reducing the difference between the modeled and synthetic strain data. The assumed permeability and compressibility were given arbitrarily. To generate abundant variations, a Gaussian correlation distribution model with a correlation length of 1 m was used. Uncorrelated distributions were realized for the permeability and compressibility fields. The distributions included some sharp spikes (e.g. 1 m), which were used to understand the spatial resolution of the inverse model.

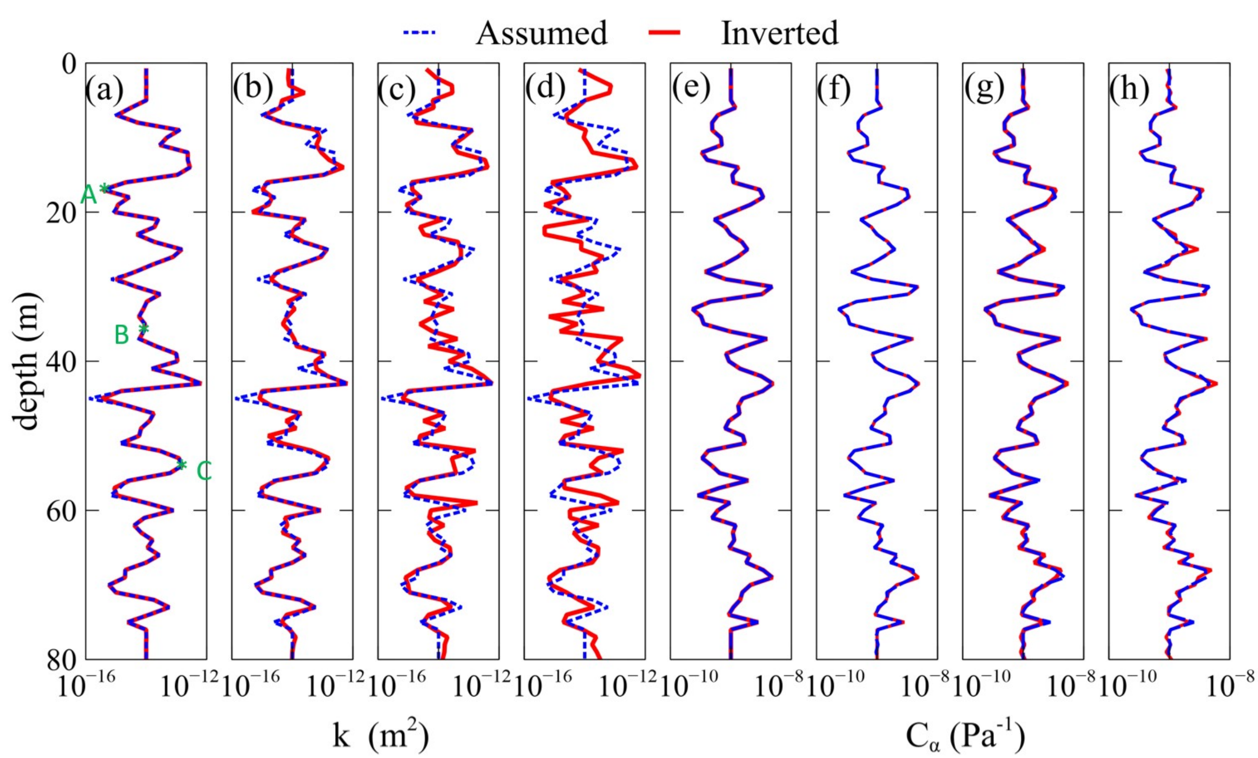

Figure 4. (a–d) Inversely estimated permeability and (e-h) compressibility profiles compared with the assumed true model parameters in the synthetic model. In the estimation of (a) and (e), the synthetic strain data without noise was used; for (b) and (f), (c) and (g), and (d) and (h), the synthetic strain data were used with added Gaussian random noise and standard deviations of 0.5, 2, and 5 με, respectively.

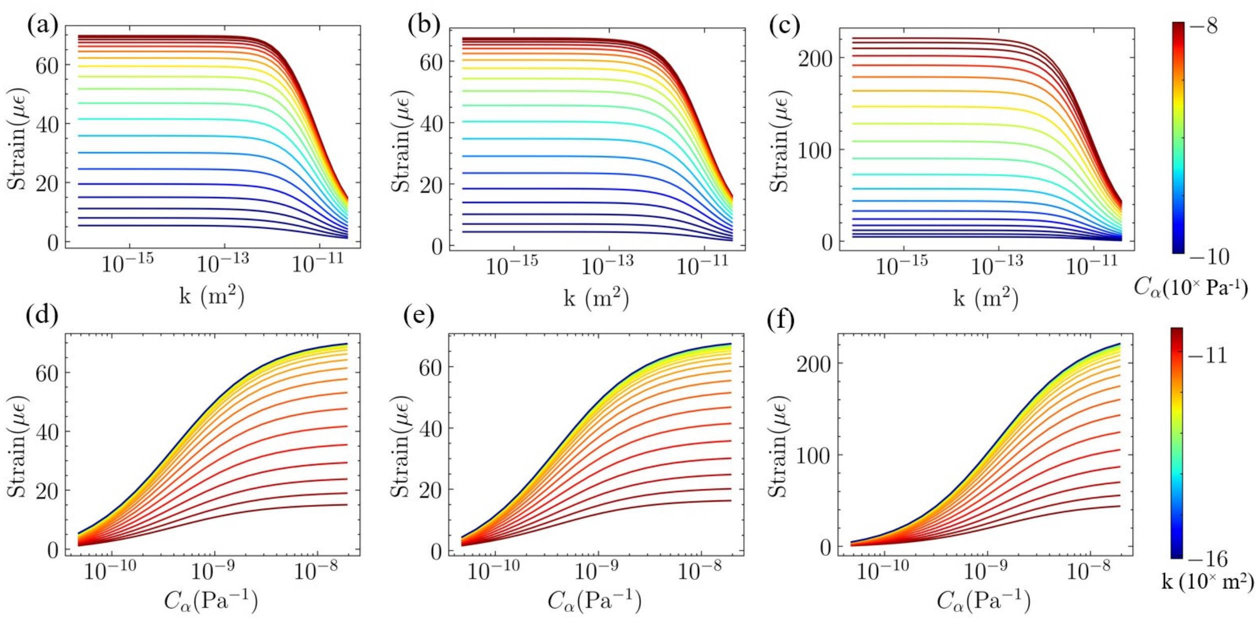

Figure 5. (a-c) Strain change with respect to permeability and (d-f) compressibility for locations A, B and C in Figure 4a.

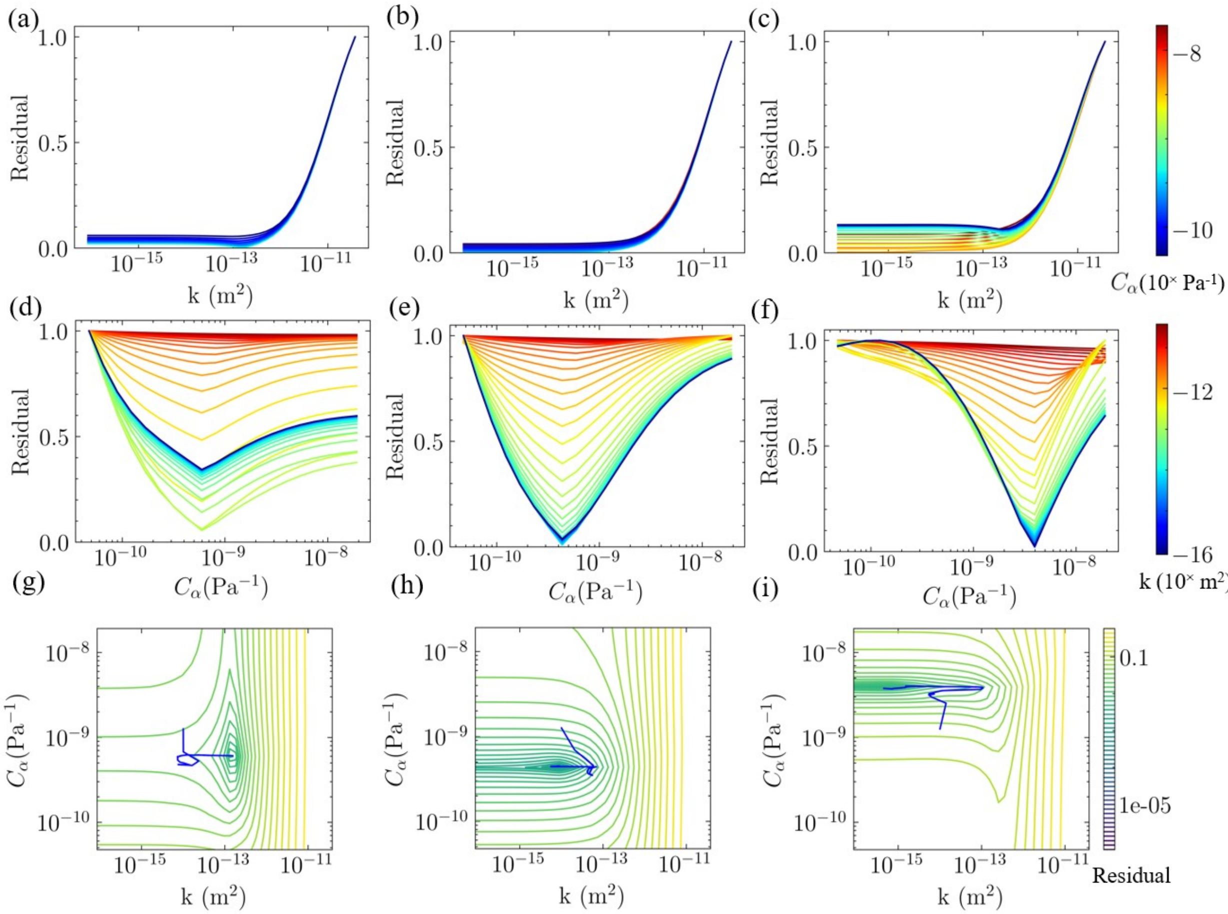

Figure 6. Normalized sensitivity of the residual of the objective function with respect to (a-c) permeability, (d-f) compressibility, and (g-i) the process of finding the best solution in the solution space for locations A, B and C in Figure 4a.

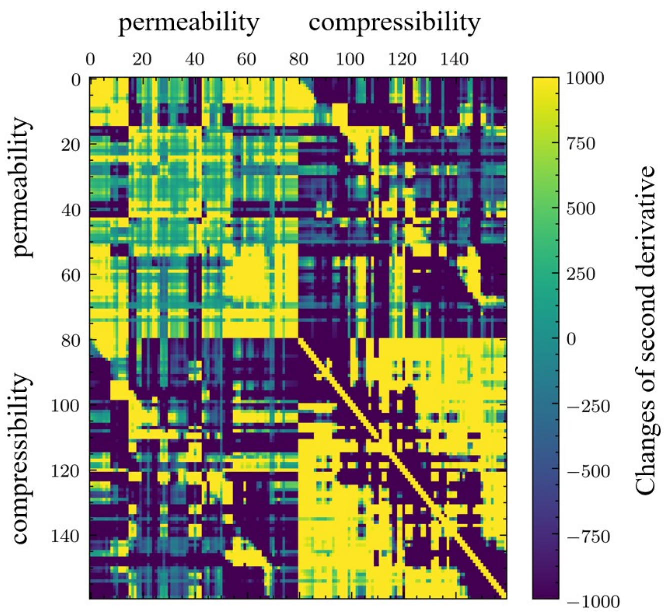

Figure 7. Approximate Hessian matrix of the objective function near the optimal solution of the synthetic study.

The sensitivities of changes in strain and the objective function (expressed by the residual between assumed and calculated strains) with respect to permeability and compressibility at several locations (Figure 4) were investigated (Figures 5 and 6 and Figure S4). The local strain change generally shows a reducing trend with an increase in permeability and an increasing trend to with an increase in compressibility. The strain sensitivity has a significant change in the higher permeability range, e.g. > 10^{-13} m^2, whereas it shows only slight variations in the lower permeability range. In contrast, the local strain shows more gradual changes in the entire range of 10^{-10} –10^{-8} Pa^{-1}. The changes in strain magnitude are different and they depend on the spatial combination of the heterogeneity in permeability and compressibility. For example, for the points

A and B (Figure 4a), the largest strain is smaller than 70 με, whereas, for point C, the strain reaches approximately 210 με (Figure S4). However, after normalization by the maximum strain change, these points show similar trends (Figure S4a–f).

Next, we identify the global minimum of the objective function in the parameter ranges (Figure 6a–i). Corresponding to the strain sensitivity, in the solution space with higher permeability in the range, the path of residual reduction to the global minimum is more distinct. However, the residual has only slight changes in the range where the permeability is not high, e.g. $< 10^{-13}$ m^2 (Figure 6a). The global minimum is less visible in the range. By constrast, the residual has obvious changes in the entire range of 10^{-10}–10^{-8} Pa^{-1} in the space of compressibility for the permeability of $< 10^{-12}$ m^2 and the global minimum is also easily identifiable. Overall, Figures 5 and 6 indicate that the minimum for permeability is not stable with respect to the addition of errors when $k < 10^{-13}$ m^2. For sensitivity changes, it should be more difficult to estimate permeability for layers with low permeability values.

When simultaneously estimating both permeability and compressibility, one concern is that the parameter crosstalk problem may affect the iterative process in finding the true optimal solution. We can observe large changes in the off-diagonal values in the permeability or compressibility block and the crosstalk blocks in the calculated approximate Hessian matrix (Figure 7). Because the two types of unknown parameters both influence the strain, permeability and compressibility both affect each other. Moreover, the effect can propagate from one location to another. Because the total water pumping rate is constrained, in the modeling, a change in the permeability of a location will not only change the local flow rate but also the flow rate at other locations, which affects the parameter estimation.

Despite these difficulties, an optimal solution for simultaneously estimating both permeability and compressibility can be obtained through inverse modeling insofar as strain data are free from noise. Figure 4a and e show the final best estimated compressibility and permeability with the assumed distribution. Most parts of the permeability structure are recovered except some local parts with small values, whereas the inversely estimated compressibility almost overlaps the assumed distribution. Particularly, because of the spatially dense coverage of strain records, even the values for very narrow spikes can be correctly estimated. The results show that the majority permeability and compressibility structures can be inversely estimated with errors of $<2\%$. The errors in low-permeability parts can be understood from the low sensitivity of the permeability values to the objective function (see Figure 6a–c), which makes it difficult for the gradient-based optimization algorithm to find the global minimum. Figure 6g–i shows the iterative process for finding the best solution.

By contrast, if the strain data contain noise (e.g.$\sigma = 0.5$ με, in Figure 4b and f), it is difficult to obtain the global optimal solution at some locations using the current gradient-based algorithm (Figure 4c and d). Because of the integrated effect of parameter crosstalk and noise, the solution may be entrapped into some local minimums near the global solution and cannot further reach the residual corresponding to the global solution. The influence becomes more severe when the noise level increases (e.g. 2 and 5 με in Figure 4e and f). This has a large impact on the permeability estimation as indicated by the distinct sensitivity changes in Figures 5 and 6. The minimum in the objective function may be not stable with respect to errors if the noise level is high (Figure 6). The influence is non-local and can propagate into other locations because of the constraint of the total flow rate. Regardless, overall, the magnitude and main structure of hydraulic parameters can be largely estimated. The results of synthetic studies demonstrate the feasibility of the proposed method with low noise. The low noise level can be guaranteed by high accuracy (0.5 με) and stability in the field measurement using DSS.

4.2 Inversion results of the field study

Next, we inversely estimated the formation permeability and compressibility for the field study. In the field model, all settings (domain, boundary conditions, elastic and fluid flow properties) were the same as the synthetic model, but we used the true observations of strain recorded by DSS. To reduce the computational dimension, we upscaled the measured strain data from 5 cm intervals to 1 m length by arithmetic average. The entire 80 m-thick formation was divided into 80 layers with 80 series of strain records and 80 × 2 unknowns of permeability and compressibility in the inversion model.

The parameter sensitivity shows similar characteristics to the synthetic study (Figure S6a–i). Similar to the synthetic study with noise, it is difficult to obtain a unique global solution by reducing the residual by the gradient-based algorithm. Instead, multiple near-optimal local solutions with similar levels of residuals exist. Moreover, because of the parameter crosstalk problem, the local solutions may be very distinct in the values of hydraulic parameters. In our tests, the inverted permeability of local solutions can have a difference of two orders of magnitude. In all these solutions, the modeled strain changes seem well consistent with the measurements (Figure 8). We selected one preferred solution with the information of the water head change in Well3 (Figure S5). The preferred solution has a good correspondence between the modelled and measured aquifer water head change (Figure S8). This implies that the additional head constraint could be helpful in mitigating the trade-off between permeability and compressibility in the inversion. The solutions in the solving space of three points (Figure 9a) are shown in Figure S6g–i.

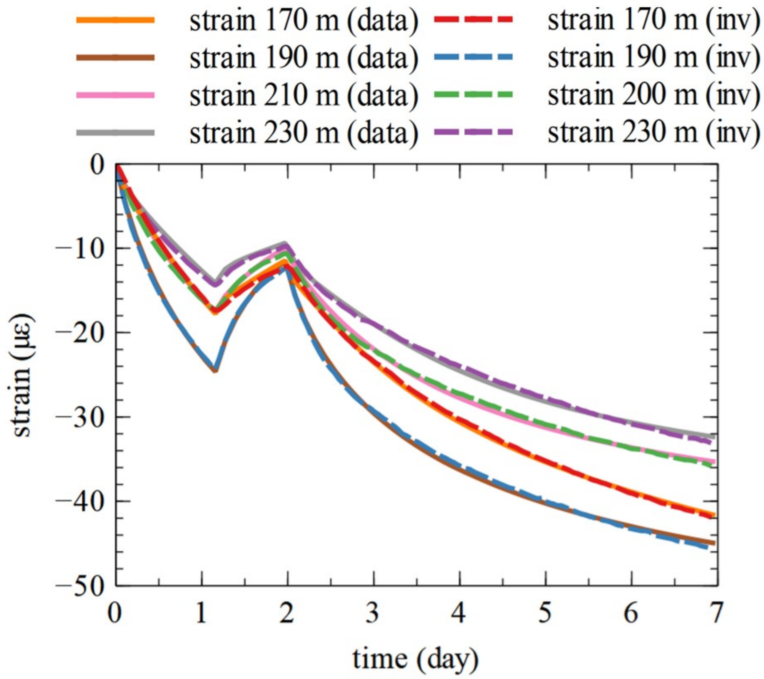

Figure 8. Modeled strain changes at several selected depths (170, 190, 210, and 230 m) of the best solution from inverse estimation compared with the field-measured strain data using DSS.

The inversely estimated permeability and compressibility (k and C_α) profiles are shown in Figure 9a and 9b. The estimated permeability ranges from approximately 0.1 mD to 1 D in different parts of the profile. There are several groups with higher permeability (>20 mD). The intervals with high and low permeability (near 190 and 215 m, respectively) are consistent with the strain peak and trough as shown in Figure 9d. Although there are some inconsistent parts, the depth intervals with higher permeability values generally point to layers that mainly comprise sandstones, as shown by the Electrical Micro Imaging (EMI) in Figure 10f. It seems that some of the low permeability intervals can be also matched to some featured spikes in the well logs (Vp, Vs and gamma ray) in Figure 10c–e. The estimated flow rate (Figure 9c) shows a similar shape to the permeability profile. The lithological changes and permeability structure determine the spatial migration of water as well as the propagation and distribution of pore fluid pressure, which further controls the formation deformation as described by poroelastic theory.

The permeability range is largely consistent with the estimated single permeability value (470 mD; Figure 9a) which is based on the data of hydraulic head changes for the entire formation of a previous study (Lei et al., 2019). Some inconsistent parts between the estimated permeability structure and EMI can be attributed to the fact that, physically, the lithological changes may only partially reflect the permeability structure. For example, there may be invisible micro-fractures that increase permeability.

The estimated compressibility generally shows a pattern similar to the spatial strain distribution; however, the changes are subtler. The compressibility varies between 3.6×10^{-10} and 2.8×10^{-9} 1/Pa along the profile. As strain changes, two parts (from 160 to 215 m and from 215 to 240 m) in the compressibility profile can be distinguished. It seems that the corresponding changes are also distinguishable from the Vp and Vs well logs.

Overall, the permeability and compressibility determine the strain pattern. Some local strain fluctuations (e.g. peaks or troughs) are predominated by the permeability structure. For a multi-layer formation, the overall changes in the aquifer pressure and deformation are partitioned to the sub-layers. Layers with high permeability and compressibility can easily develop greater deformation and thus dominate the deformation pattern. Hydromechanically, the lithological layers may be grouped into several units. The inversely estimated hydraulic parameters can be generally and reasonably interpreted from the geological information.

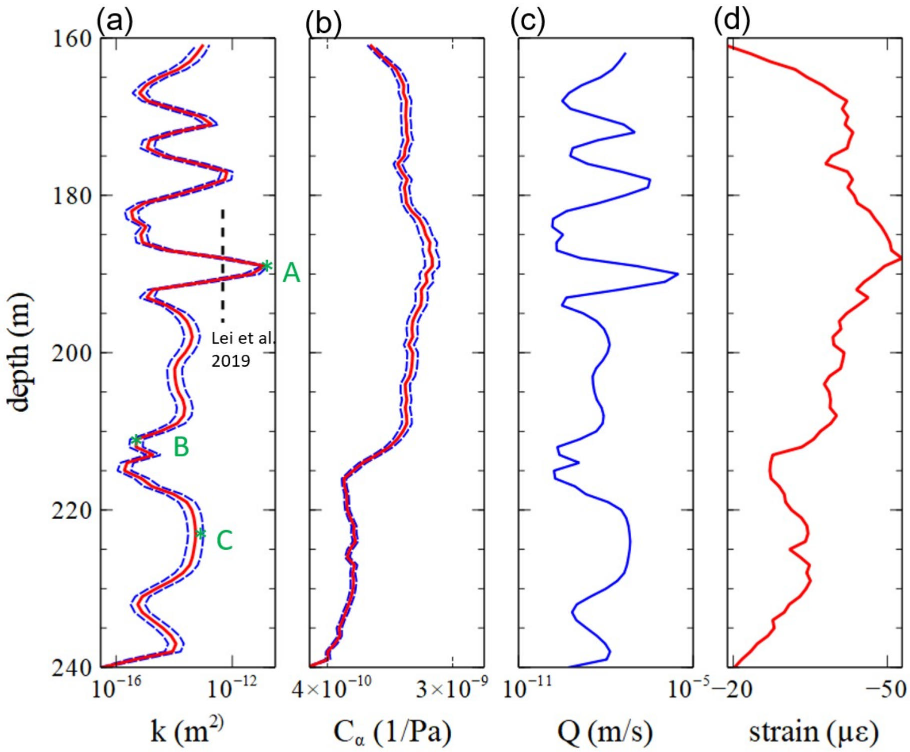

(a)
(b)
(c)
(d)
160
180
200
220
240
depth (m)
A
B
C
Lei et al.
2019
10^{-16}
10^{-12}
k (m^2)
4×10^{-10}
3×10^{-9}
C_α (1/Pa)
10^{-11}
10^{-5}
Q (m/s)
−20
−50
strain (με)

Figure 9. The inversely estimated profiles of (a) permeability, (b) compressibility and (c) flow rate (the Darcy velocity) with (d) the strain profile in the final. The dashed lines in (a) and (b) indicate the uncertainty of one standard deviation in the estimation obtained from the approximation of the Hessian matrix.

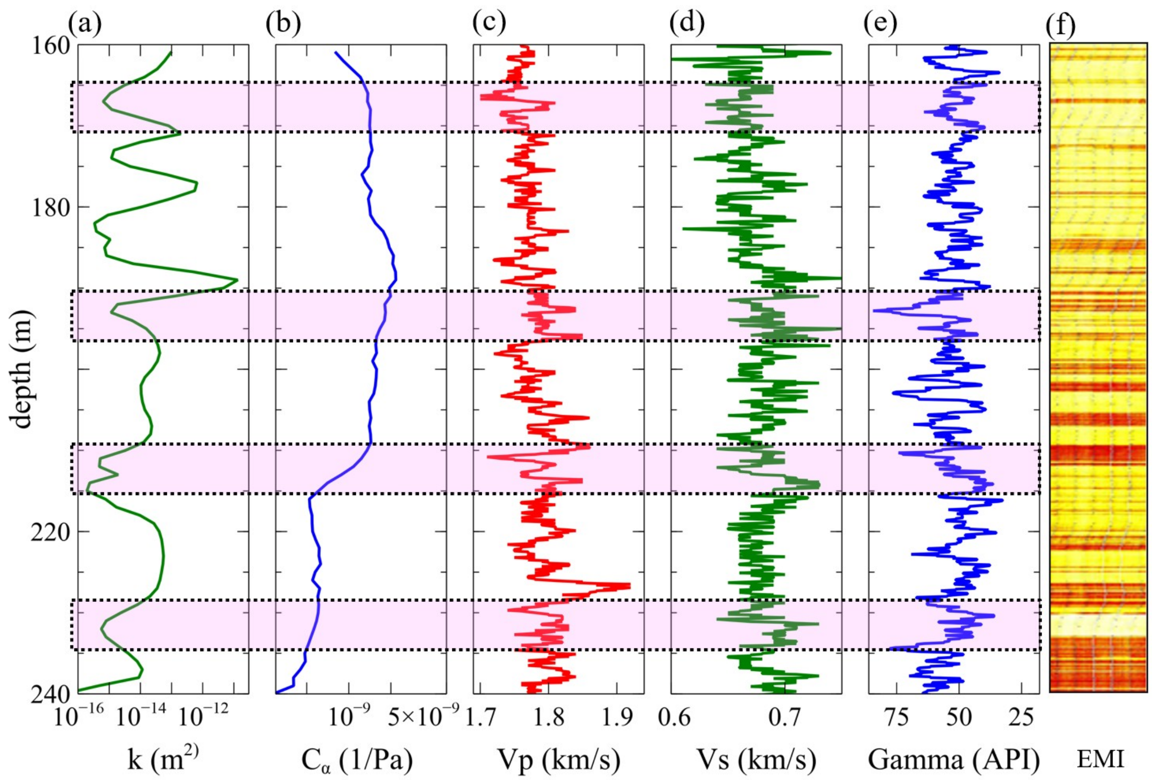

Figure 10. The inversely estimated profiles of (a) permeability and (b) compressibility, with well logs of (c) compressive wave velocity, (d) shear wave velocity, (e) gamma ray, and (f) EMI of the well showing the lithological structure (sandstone–mudstone alternations).

5. Discussions and conclusions

In conventional studies, one primary issue causing difficulty in obtaining hydraulic parameters is the measurement of either in situ formation pressure or hydraulic head for multilayer formation. It is not practical to measure the hydraulic head at each depth location of each layer in a well (or in many wells) when the formation develops many layers, such as the sandstone–mud alternations in this study. The measurement of in situ formation pressure also has an intrinsic problem in that it is not feasible to embed many discrete pressure sensors in the formation along a wellbore.

Unlike conventional pressure sensors, as shown by this study, an optical fiber cable placed in the cement between the well casing and the sedimentary formation can be deployed for the distributed sensing of hydromechanical responses with high fidelity measurements. Although the measured parameter is strain and not pressure, under the linear poroelastic deformation mechanism (Biot, 1941; Cheng, 2016; Rice & Cleary, 1976; Wang, 2017), the pore pressure induced strain change is closely associated with changes in pore pressure (Berg et al., 2015; Burbey, 2001; Hesse & Stadler, 2014).

As demonstrated in this study, strain data can provide a similar function to pore pressure. The recorded strain data clearly show the spatial distribution and migration of pore pressure perturbations. Parameter estimation using DSS data can provide additional benefits with detailed information of formation properties in the vertical direction that are beyond previously mentioned geomechanical applications. The information should be useful for understanding the contribution of each layer to the overall fluid transport and pressure evolution (Figure 9c and d), as well as for determining appropriate fluid injection or extraction strategy (such as interval and rate) in underground fluid storage (e.g., CO_2 storage) projects. The responses at the initial stages can be used to characterize reservoir permeability and compressibility structure, which could assist in continued injection design and pressure management to avoid potential geomechanical risks (Buscheck et al., 2012).

One of the limitations of the proposed method is concerned with the estimation of layers with low-permeability values. This can be attributed to the low sensitivity of strain changes for a permeability < 10^{-13} m^2. Particularly, when a larger measurement noise (σ = 5 $\mu\varepsilon$) is added in the synthetic study, it is difficult to further reduce the residual of the objective function and obtain the global solution, and the estimation of permeability becomes unstable using the current gradient-based minimization method. In the field case, the errors coming from upscaling using the arithmetic averaging method may also affect the parameter estimation. Because of the combined effect of parameter crosstalk and data noise, the current solution may be solely a near-optimal solution. A choice of other inversion methods (such as the adjoint-based method; Vasco and Mail, 2020) and global optimization methods (Comola et al., 2016; Jones, et al., 1998), or a better regularization technique (Aster et al., 2018; Menke, 2018; Ren & Kalscheuer, 2020) may improve the solution.

Additionally, some unconsidered physical mechanisms may also affect the modelling. These may include the pressure or strain dependent permeability relationship, small inelastic contribution, depth dependent Biot's coefficient, anisotropy in the properties, and neglected changes in Poisson's ratio. Because there is no constraint of lateral strain, we only used one constant value for Poisson's ratio. A future survey with measurements of lateral strain (e.g. by a helical installation of the fiber cable) may be helpful for improved estimation.

In this study, for the experimental design and available data, we have attemped to simultaneously estimate both permeability and compressibility. The simultaneous estimation of two parameters significantly increases the inversion difficulty compared with estimating one parameter. In practice, the compressibility can be constrained first by an improved testing strategy. For example, two or more steady-state steps resulting from constant head testing can be used to analytically calculate compressibility, making the estimation of permeability less challenging. By constant head testing, the constraint from the total flow rate can be removed, and thus, the inverse modeling can be made effortless.

Furthermore, we approximated the aquifer as a one-dimensional layered property model (but with an axisymmetric two-dimensional model) and neglected lateral changes for simplicity. The approximation may result in model errors. A cross-well hydraulic tomography (Rucci et al., 2010; Vasco et al., 2014), using the information of onset time, amplitude or phase changes in strain signals, may be helpful for resolving two-dimensional variations, as well as for reducing modeling errors and extending the method to more complex aquifers. The use of DSS makes cross-well tests easier to conduct; it also makes it easier to view time-lapse changes between tests.

The high-quality DSS data acquired in the field study and the good correspondence between strain and formation pressure suggest that the recorded strain can be attributed to formation deformation. One concern is that it is unclear whether the measured strain is partially or fully representative of the formation deformation. Some studies have considered the strain transfer problem for unconsolidated formation with loose coupling between formation and cement (Zhang et al., 2020). However, according to Becker et al. (2018), for a stiff rock formation with good coupling between formation and cement (without slippage), the strain measurement by DSS represents formation deformation.

Another concern is related to the effect of parameter correlation between permeability and compressibility in the simultaneous estimation. The parameter correlation could lead to problems in hydraulic tomographic studies because the data used to estimate spatial parameters in the underdetermined problems were limited. However, in our study, we find that the estimations are unaffected when intentionally setting correlated or uncorrelated permeability and compressibility fields in synthetic testing. In our method, we calculated parameters with the strong constraint from the measurement of each individual layer. The permeability and compressibility of each layer are mostly constrained by the strain changes in each layer. Within each layer, the response is similar to that of conventional well testing with an assumption of uniform properties between wells; however, the response is still influenced by neighboring layers and the constraint from the total flow rate.

Acknowledgments

We thank Dr. D. Vasco, three anomalous reviewers, and the associate editor for their critical comments and suggestions towards improving the manuscript. This paper is based on results obtained from a project (JPNP18006) commissioned by the New Energy and Industrial Technology Development Organization (NEDO) and the Ministry of Economy, Trade and Industry (METI) of Japan. This research is partially supported by Initiative on Promotion of Supercomputing for Young or Women Researchers, Supercomputing Division, Information Technology Center, The University of Tokyo (for the usage of supercomputer system).

Data Availability Statement

The strain data are available at http://dx.doi.org/10.6084/m9.figshare.12178656.

References

Alghamdi, A., Hesse, M. A., Chen, J., & Ghattas, O. (2020). Bayesian Poroelastic Aquifer Characterization From InSAR Surface Deformation Data. Part I: Maximum A Posteriori Estimate. Water Resources Research, 56(10), e2020WR027391. https://doi.org/https://doi.org/10.1029/2020WR027391

Anderson, M. P., Woessner, W. W., & Hunt, R. J. (2015). *Applied groundwater modeling: simulation of flow and advective transport*. Academic press.

Aster, R. C., Borchers, B., & Thurber, C. H. (2018). *Parameter estimation and inverse problems*.

Elsevier.

Bear, J., & Verruijt, A. (2012). *Modeling groundwater flow and pollution* (Vol. 2). Springer Science & Business Media.

Becker, M W, Georgian, T., Ambrose, H., Siniscalchi, J., & Fredrick, K. (2004). Estimating flow and flux of ground water discharge using water temperature and velocity. *Journal of Hydrology*, *296*(1), 221–233. https://doi.org/https://doi.org/10.1016/j.jhydrol.2004.03.025

Becker, M W, Coleman, T. I., & Ciervo, C. C. (2020). Distributed Acoustic Sensing (DAS) as a Distributed Hydraulic Sensor in Fractured Bedrock. *Water Resources Research*, e2020WR028140.

Becker, M W, Ciervo, C., & Coleman, T. (2018). A Slimhole Approach to Measuring Distributed Hydromechanical Strain in Fractured Geothermal Reservoirs. In *Proceedings of the 43rd Workshop on Geothermal Reservoir Engineering Stanford University, Palo Alto, CA, USA* (pp. 12–14).

Bohloli, B., Bjørnarå, T. I., Park, J., & Rucci, A. (2018). Can we use surface uplift data for reservoir performance monitoring? A case study from In Salah, Algeria. *International Journal of Greenhouse Gas Control*, *76*(June 2017), 200–207. https://doi.org/10.1016/j.ijggc.2018.06.024

Branch, M. A., Coleman, T. F., & Li, Y. (1999). A subspace, interior, and conjugate gradient method for large-scale bound-constrained minimization problems. *SIAM Journal on Scientific Computing*, *21*(1), 1–23.

Buscheck, T. A., Sun, Y., Chen, M., Hao, Y., Wolery, T. J., Bourcier, W. L., et al. (2012). Active CO2 reservoir management for carbon storage: Analysis of operational strategies to relieve pressure buildup and improve injectivity. *International Journal of Greenhouse Gas Control*, *6*, 230–245.

Commer, M., Pride, S. R., Vasco, D. W., Finsterle, S., & Kowalsky, M. B. (2020). Imaging of a fluid injection process using geophysical data—A didactic example. Geophysics, 85(2), W1–W16.

Comola, F., Janna, C., Lovison, A., Minini, M., Tamburini, A., & Teatini, P. (2016). Efficient global optimization of reservoir geomechanical parameters based on synthetic aperture radar-derived ground displacements. Geophysics, 81(3), M23–M33. https://doi.org/10.1190/GEO2015-0402.1

Gleeson, T., Wada, Y., Bierkens, M. F. P., & Van Beek, L. P. H. (2012). Water balance of global aquifers revealed by groundwater footprint. *Nature*, *488*(7410), 197–200.

Gottlieb, J., & Dietrich, P. (1995). Identification of the permeability distribution in soil by hydraulic tomography. *Inverse Problems*, *11*(2), 353.

Guglielmi, Y., Nussbaum, C., Jeanne, P., Rutqvist, J., Cappa, F., & Birkholzer, J. (2020). Complexity of Fault Rupture and Fluid Leakage in Shale: Insights From a Controlled Fault Activation Experiment. *Journal of Geophysical Research: Solid Earth*, *125*(2), e2019JB017781. https://doi.org/10.1029/2019JB017781

Hochstetler, D. L., Barrash, W., Leven, C., Cardiff, M., Chidichimo, F., & Kitanidis, P. K. (2016). Hydraulic tomography: Continuity and discontinuity of high−K and low−K zones. *Groundwater*, *54*(2), 171–185.

Horiguchi, Y. (1998). Outline of water-dissolved natural gas field in Chiba Prefecture. *Journal of the Japanese Association for Petroleum Technology*, *63*(6), 475–484. https://doi.org/10.3720/japt.63.475

Huntley, D. (1986). Relations between permeability and electrical resistivity in granular aquifers. *Groundwater*, *24*(4), 466–474.

Hsieh, P. A., Bredehoeft, J. D., & Farr, J. M. (1987). Determination of aquifer transmissivity from Earth tide analysis. Water Resources Research, 23(10), 1824–1832.

Istok, J. D., & Dawson, K. J. (2014). *Aquifer testing: design and analysis of pumping and slug* *tests*. CRC Press.

Jardani, A., and A. Revil (2009), Stochastic joint inversion of temperature and self−potential data, Geophys. J. Int., 179(1), 640– 654, doi:10.1111/j.1365−246X.2009.04295.x.

Jha, B., Bottazzi, F., Wojcik, R., Coccia, M., Bechor, N., McLaughlin, D., et al. (2015). Reservoir characterization in an underground gas storage field using joint inversion of flow and geodetic data. *International Journal for Numerical and Analytical Methods in Geomechanics*, *39*(14), 1619–1638.

Jiang, G., Qiao, X., Wang, X., Lu, R., Liu, L., Yang, H., et al. (2020). GPS observed horizontal ground extension at the Hutubi (China) underground gas storage facility and its application to geomechanical modeling for induced seismicity. *Earth and Planetary Science Letters*, *530*, 115943. https://doi.org/https://doi.org/10.1016/j.epsl.2019.115943

Jiménez, S., Brauchler, R., Hu, R., Hu, L., Schmidt, S., Ptak, T., & Bayer, P. (2015). Prediction of solute transport in a heterogeneous aquifer utilizing hydraulic conductivity and specific storage tomograms. *Water Resources Research*, *51*(7), 5504–5520.

Jones, D. R., Schonlau, M., & Welch, W. J. (1998). Efficient global optimization of expensive black-box functions. Journal of Global Optimization, 13(4), 455–492.

Jousset, P., Reinsch, T., Ryberg, T., Blanck, H., Clarke, A., Aghayev, R., et al. (2018). Dynamic strain determination using fibre-optic cables allows imaging of seismological and structural features. *Nature Communications*, *9*(1). https://doi.org/10.1038/s41467-018-04860-y

Keranen, K. M., Weingarten, M., Abers, G. A., Bekins, B. A., & Ge, S. (2014). Sharp increase in central Oklahoma seismicity since 2008 induced by massive wastewater injection. *Science*, *345*(6195), 448–451. https://doi.org/10.1126/science.1255802

Kishida, K., Yamauchi, Y., & Guzik, A. (2014). Study of optical fibers strain-temperature sensitivities using hybrid Brillouin-Rayleigh System. *Photonic Sensors*, *4*(1), 1–11.

Kitanidis, P. K. (1997). *Introduction to geostatistics: applications in hydrogeology*. Cambridge university press.

Lei, X., Xue, Z., & Hashimoto, T. (2019). Fiber optic sensing for geomechanical monitoring:(2)-distributed strain measurements at a pumping test and geomechanical modeling of deformation of reservoir rocks. *Applied Sciences*, *9*(3), 417.

Lei, X., Su, J., & Wang, Z. (2020). Growing seismicity in the Sichuan Basin and its association with industrial activities. Science China Earth Sciences, 1–28.

Liang, L., Abubakar, A., & Habashy, T. M. (2016). Reservoir property mapping and monitoring from joint inversion of time-lapse seismic, electromagnetic, and production data. Geophysics, 81(5), ID73–ID84.

Maldaner, C. H., Munn, J. D., Coleman, T. I., Molson, J. W., & Parker, B. L. (2019). Groundwater Flow Quantification in Fractured Rock Boreholes Using Active Distributed Temperature Sensing Under Natural Gradient Conditions. *Water Resources Research*, *55*(4), 3285–3306. https://doi.org/10.1029/2018WR024319

Medina, R., Pham, C., Plumlee, M. H., Hutchinson, A., Becker, M. W., & O'Connell, P. J. (2020). Distributed temperature sensing to measure infiltration rates across a groundwater recharge basin. *Groundwater*, *n/a*(n/a). https://doi.org/10.1111/gwat.13007

Menke, W. (2018). *Geophysical data analysis: Discrete inverse theory*. Academic press.

Miller, M. M., Shirzaei, M., & Argus, D. (2017). Aquifer Mechanical Properties and Decelerated Compaction in Tucson, Arizona. *Journal of Geophysical Research: Solid Earth*, *122*(10), 8402–8416. https://doi.org/10.1002/2017JB014531

Murdoch, L. C., Germanovich, L. N., DeWolf, S. J., Moysey, S. M. J., Hanna, A. C., Kim, S., & Duncan, R. G. (2020). Feasibility of using in situ deformation to monitor CO2 storage. *International Journal of Greenhouse Gas Control*, *93*(September 2018), 102853. https://doi.org/10.1016/j.ijggc.2019.102853

Wilkins, A., Green, C.P., & Ennis-King, J. (2020). PorousFlow: a multiphysics simulation code for coupled problems in porous media. Journal of Open Source Software, *5*(55), 2176. https://doi.org/10.21105/joss.02176

Ren, Z., & Kalscheuer, T. (2020). Uncertainty and resolution analysis of 2D and 3D inversion models computed from geophysical electromagnetic data. Surveys in Geophysics, 41,47–112. https://doi.org/10.1007/s10712−019−09567−3

Rice, J. R., & Cleary, M. P. (1976). Some basic stress diffusion solutions for fluid−saturated elastic porous media with compressible constituents. Reviews of Geophysics, 14(2), 227–241.

Rucci, A., Vasco, D. W., & Novali, F. (2010). Fluid pressure arrival-time tomography: Estimation and assessment in the presence of inequality constraints with an application to production at the Krechba field, Algeria. Geophysics, 75(6), O39–O55.

Schenato, L. (2017). A review of distributed fibre optic sensors for geo-hydrological applications. *Applied Sciences (Switzerland)*. https://doi.org/10.3390/app7090896

Shirzaei, M., Ellsworth, W. L., Tiampo, K. F., González, P. J., & Manga, M. (2016). Surface uplift and time-dependent seismic hazard due to fluid injection in eastern Texas. *Science*, *353*(6306), 1416–1419.

Shirzaei, M., Manga, M., & Zhai, G. (2019). Hydraulic properties of injection formations constrained by surface deformation. *Earth and Planetary Science Letters*, *515*, 125–134. https://doi.org/10.1016/j.epsl.2019.03.025

Sun, Y., Xue, Z., Hashimoto, T., Lei, X., & Zhang, Y. (2020). Distributed Fiber Optic Sensing System for Well-based Monitoring Water Injection Tests — A Geomechanical Responses Perspective. *Water Resouces Research*, *56*, 1–30.

Vasco, D W. (2018). An extended trajectory mechanics approach for calculating the path of a pressure transient: Derivation and illustration. *Water Resources Research*, *54*(4), 2642–2660.

Vasco, D W, Datta−Gupta, A., & Long, J. C. S. (1997). Resolution and uncertainty in hydrologic characterization. *Water Resources Research*, *33*(3), 379–397.

Vasco, D W, Ferretti, A., & Novali, F. (2008). Reservoir monitoring and characterization using satellite geodetic data: Interferometric synthetic aperture radar observations from the Krechba field, Algeria. *Geophysics*, *73*(6), WA113–WA122.

Vasco, D. W., & Mali, G. (2020). On the use of adjoints in the inversion of observed quasi-static deformation. Geophysical Journal International, 224(2), 896–908. https://doi.org/10.1093/gji/ggaa481

Vasco, D W, Rucci, A., Ferretti, A., Novali, F., Bissell, R. C., Ringrose, P. S., et al. (2010). Satellite‐based measurements of surface deformation reveal fluid flow associated with the geological storage of carbon dioxide. *Geophysical Research Letters*, *37*(3).

Vasco, D. W., Daley, T. M., & Bakulin, A. (2014). Utilizing the onset of time-lapse changes: A robust basis for reservoir monitoring and characterization. Geophysical Journal International, 197(1), 542–556.

Vasco, Donald W, Doetsch, J., & Brauchler, R. (2019). An extended trajectory-mechanics approach for calculating the path of a pressure transient: travel-time tomography. *Hydrology and Earth System Sciences*, *23*(11), 4541–4560.

Verdon, J. P., Stork, A. L., Bissell, R. C., Bond, C. E., & Werner, M. J. (2015). Simulation of seismic events induced by CO2 injection at In Salah, Algeria. *Earth and Planetary Science Letters*, *426*, 118–129. https://doi.org/https://doi.org/10.1016/j.epsl.2015.06.029

Virtanen, P., Gommers, R., Oliphant, T. E., Haberland, M., Reddy, T., Cournapeau, D., et al. (2020). SciPy 1.0: fundamental algorithms for scientific computing in Python. *Nature Methods*, *17*(3), 261–272.

Wang, C., Doan, M., Xue, L., & Barbour, A. J. (2018). Tidal response of groundwater in a leaky aquifer—Application to Oklahoma. Water Resources Research, 54(10), 8019–8033.

Wang, H. F. (2017). *Theory of linear poroelasticity with applications to geomechanics and* *hydrogeology*. Princeton University Press.

Yamamoto, T., Nye, T., & Kuru, M. (1995). Imaging the permeability structure of a limestone aquifer by crosswell acoustic tomography. *Geophysics*, *60*(6), 1634–1645.

Yeh, T. J., & Liu, S. (2000). Hydraulic tomography: Development of a new aquifer test method. *Water Resources Research*, *36*(8), 2095–2105.

Zhang, Y., & Xue, Z. (2019). Deformation−Based Monitoring of Water Migration in Rocks Using Distributed Fiber Optic Strain Sensing: A Laboratory Study. *Water Resources Research*, *55*(11), 8368–8383.

Zhang, Y., Xue, Z., Park, H., Shi, J., Kiyama, T., Lei, X., et al. (2019). Tracking CO2 Plumes in Clay−Rich Rock by Distributed Fiber Optic Strain Sensing (DFOSS): A Laboratory Demonstration. *Water Resources Research*, *55*(1), 856–867.

Zhang, Y., Lei, X., Hashimoto, T., & Xue, Z. (2020). In situ hydromechanical responses during well drilling recorded by distributed fiber-optic strain sensing. *Solid Earth Discussions*, 1–15. https://doi.org/10.5194/se-2020-61

Journal of Geophysical Research: Solid Earth

Supporting Information for

Towards retrieving distributed aquifer hydraulic parameters from distributed strain sensing

Yi Zhang[1 *], Xinglin Lei[2], Tsutomu Hashimoto[1], Ziqiu Xue[1]

Corresponding author: zhangyi@rite.or.jp

[1] Research Institute of Innovative Technology for the Earth (RITE), 9-2, Kizugawadai, Kizugawa-Shi, Kyoto, 619-0292 Japan.

[2] Geological Survey of Japan, National Institute of Advanced Industrial Science and Technology, AIST Central #7, Higashi 1-1-1, Tsukuba, Ibaraki 305-8567, Japan.

Contents of this file

Depth（m）			Cores
150.0	~	153.0	
153.0	~	156.0	
156.0	~	159.0	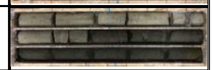
159.0	~	162.0	
162.0	~	165.0	
165.0	~	168.0	
168.0	~	171.0	
171.0	~	174.0	
174.0	~	177.0	
177.0	~	180.0	
180.0	~	183.0	
183.0	~	186.0	
186.0	~	189.0	
189.0	~	192.0	
192.0	~	195.0	
195.0	~	198.0	
198.0	~	201.0	
201.0	~	204.0	
204.0	~	207.0	
207.0	~	210.0	
210.0	~	213.0	
213.0	~	216.0	
216.0	~	219.0	
219.0	~	222.0	
222.0	~	225.0	

225.0	~	228.0	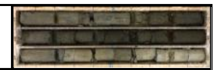
228.0	~	231.0	
231.0	~	234.0	
234.0	~	237.0	
237.0	~	240.0	

Figure S1. The sampled cores during drilling the wellbore showing the sandstone with mud and siltstone alternations.

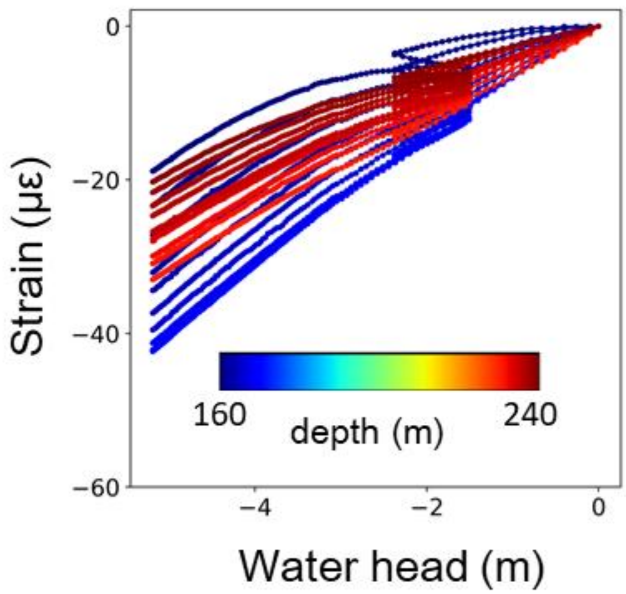

Figure S2. Nonlinear strain changes with respect to water head in depth intervals between 160 m and 170 m, and 230 m and 240 m.

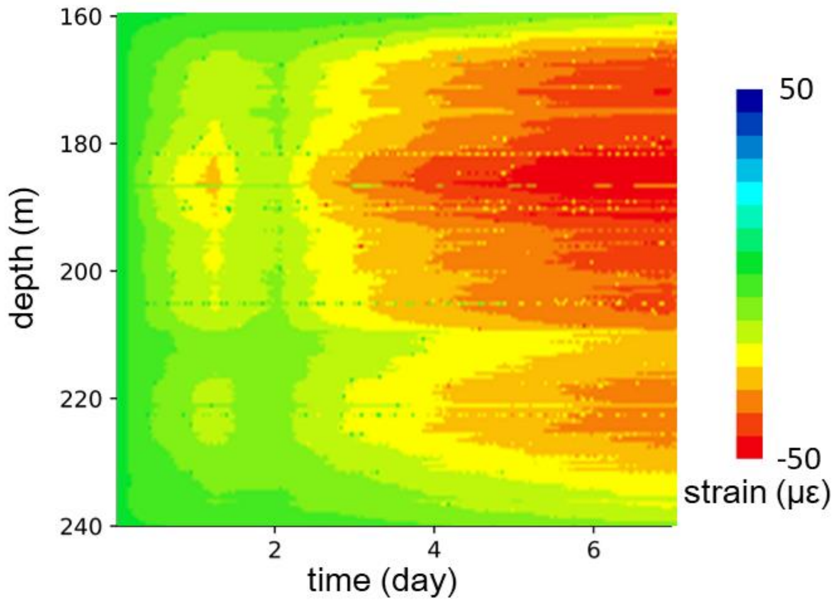

Figure S3. Raw strain data were recorded by distributed fiber optic strain sensing during water extraction. At some depths, the strain errors due to incorrectly matching Rayleigh scattering power spectra using the cross-correlation method are shown.

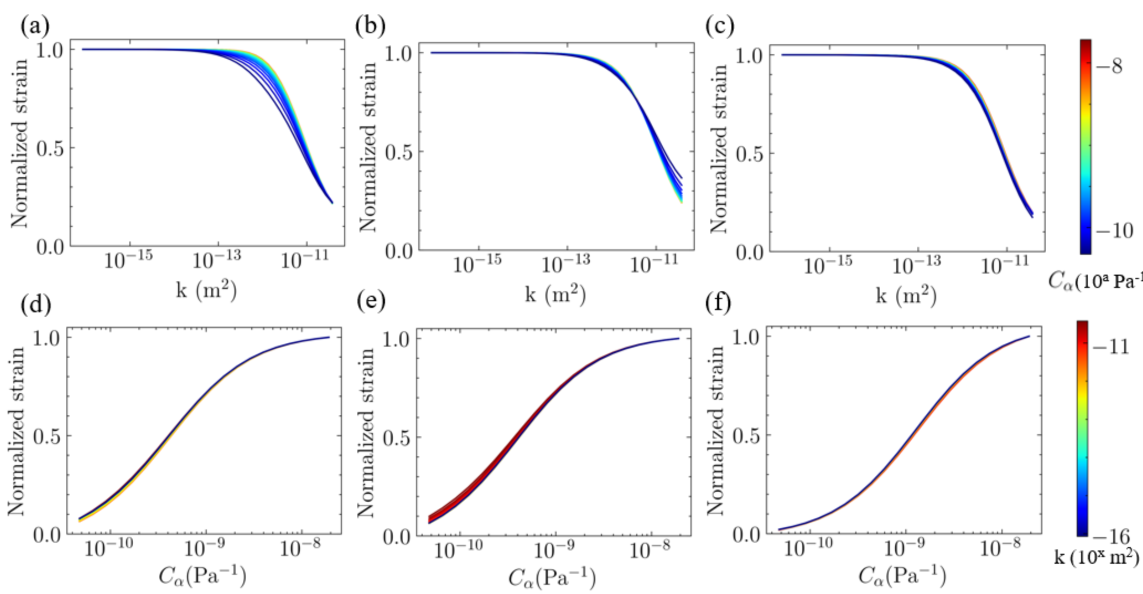

Figure S4. Normalized strain change with respect to permeability (k) (a-c) and compressibility (C_α) (d-f) for locations A, B and C in Figure 4a.

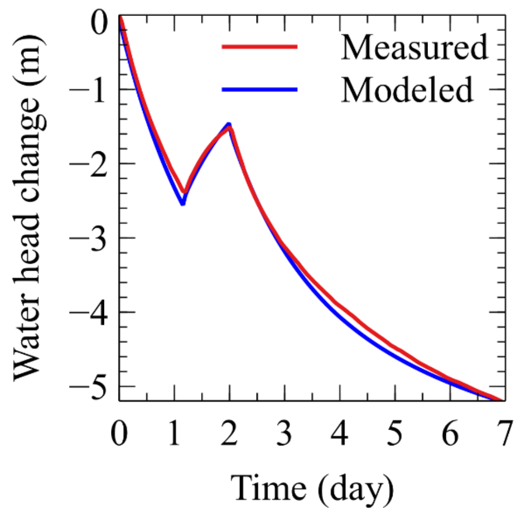

Figure S5. Comparison of the modeled water head change with the measured one.

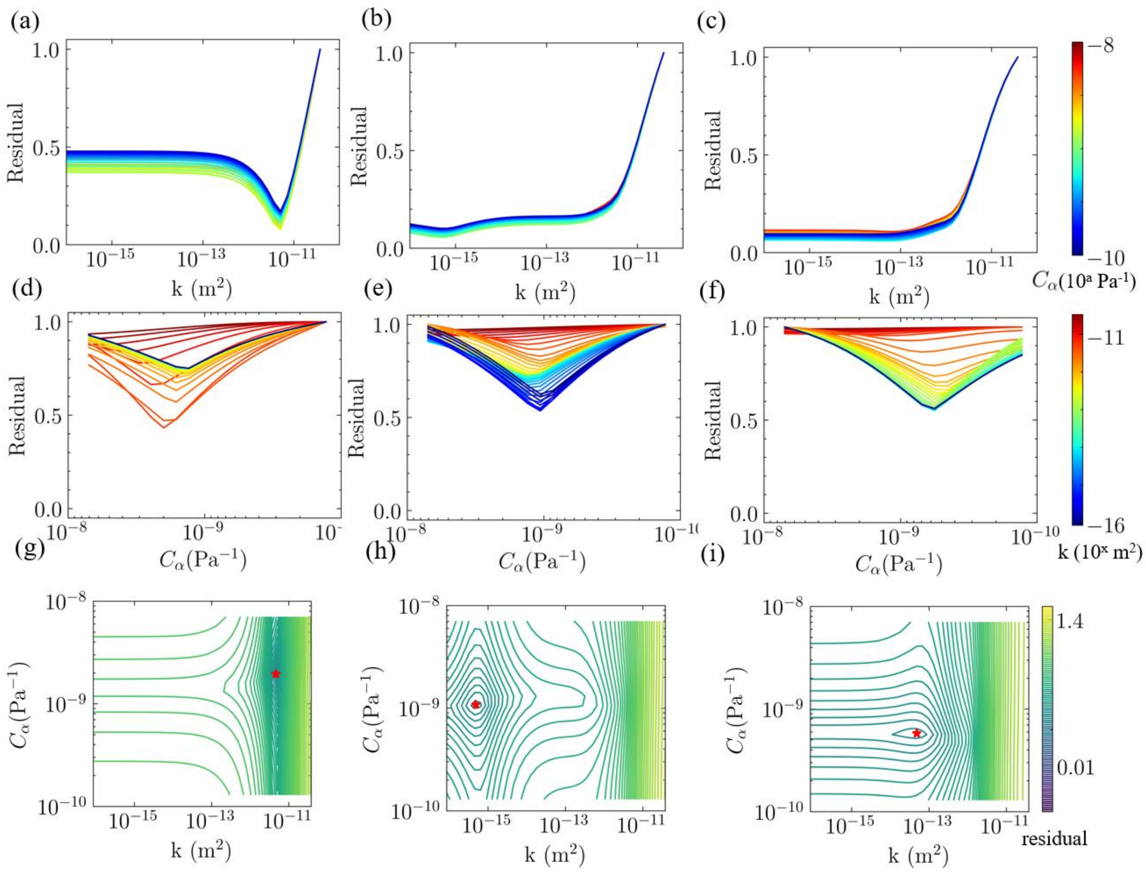

Figure S6. Normalized sensitivity of residual with respect to permeability (k) (a-c), compressibility (C_α) (d-f), and the process of finding best solution in the solution space (g-i) for locations A, B and C in Figure 9a.